AIMS Mathematics, 10(10): 23715–23737.
DOI: 10.3934/math.20251054
Received: 28 July 2025
Revised: 17 September 2025
Accepted: 19 September 2025
Published: 17 October 2025

https://www.aimspress.com/journal/Math

Research article

Dynamic response of fibrillar adhesive floating breakwater near a porous structure and Gaussian oscillatory seabed with added mass and damping effects

S. Sujana Praisilin[1], Chandru Muthusamy[1,*] and Higinio Ramos[2,3,*]

[1] Department of Mathematics, School of Advanced Sciences, Vellore Institute of Technology, Vellore 632014, Tamil Nadu, India
[2] Scientific Computing Group, University of Salamanca, Plaza de la Merced, 37008 Salamanca, Spain
[3] Department of Applied Mathematics, Escuela Politécnica Superior de Zamora, University of Salamanca, Campus Viriato, 49022 Zamora, Spain

* **Correspondence:** Email: leochandru@gmail.com, higra@usal.es.

Abstract: This study examines the dynamic response of a fibrillar adhesive floating breakwater positioned near a porous structure at a finite distance from Gaussian undulating seabed. The problem is addressed using linearized water wave theory, with numerical simulations based on the multi-domain boundary element method. The study primarily focuses on the analysis of crucial elements such as the added mass and damping coefficients associated with heave, surge, and pitch motions, considering the influence of both wave and structural parameters. Validation against existing literature confirms the accuracy and reliability of the proposed method. The study reveals that an increase in the number of seabed ripples leads to higher added mass and damping coefficients, particularly at larger wave incidence angles. Further, the frictional interaction between the water and the porous structure modifies the added mass coefficient, resulting in a shift in the resonance peak and significantly affecting the dynamic response of the breakwater. Moreover, surge and pitch motions are highly damped in intermediate waves as the porosity of the structure decreases.

Keywords: fibrillar adhesive floating breakwater; Gaussian oscillatory seabed; added mass; damping coefficient; multi-domain boundary element method

1. Introduction

As coastal regions increasingly face environmental challenges such as rising sea levels and more intense storm events, the need for robust and adaptable coastal defenses becomes paramount. In

addition, the dynamics of rigid bodies and fluid motion in the time domain are critical factors in addressing the transient movement of a floating structures [1]. Despite various conventional rigid structures developed near shorelines, intricate rigid structures are proving to be crucial in coastal infrastructure [2, 3]. Consequently, the design of these rigid breakwaters is of great importance for ensuring effective wave deformation and mitigating motion response [4]. In this scenario, novel types of floating breakwaters have recently emerged. In particular, the application of bio-inspired paradigms in coastal engineering presents an opportunity for obtaining strategies, new principles, and methodologies for developing more ecologically sustainable defences [5]. In addition, the interaction of waves with variable seabed topography is essential for understanding wave-induced mass transfer, which generates sand ripples of varying wavelengths [6]. Thus, this study examines the motion response of an intricate bio-inspired breakwater, combining rigid and porous structural elements under irregular bathymetry. Moreover, these intricate breakwater systems can integrate multiple functionalities, including transportation links, storage hubs, airstrips, renewable energy systems, defense facilities, and recreational spaces with residential capabilities.

Coastal engineers often use rigid breakwaters to protect shorelines and sea barriers from the damaging impact of waves. The efficiency of such structures largely depends on their interaction with incoming waves. According to [7], rigid barriers can generate pronounced harmonics on the lee side due to their role as scattering sources for gravity waves. Williams et al. [8] discovered that the wave reflection performance of dual-pontoon floating structures was notably affected by their draft, spacing, and width. The study further noted that for higher frequencies (wave number greater than 3.2), the structure proved to be most effective when the spacing between pontoons increased. Further, Syed and Mani [9] explored a floating breakwater system comprising triple pontoons connected rigidly and spaced equally. According to the findings, the system performed optimally in suppressing incident waves when the draft was minimal. Motion response across multiple degrees of freedom remains a significant area of study in ocean engineering. Gesraha [10] noted that the twin-pontoon arrangement surpasses the single pontoons due to increased stability from a broader foundation created by the wider spacing between the pontoons, which minimizes large roll and heave responses. Diamantoulaki et al. [11] analyzed the effectiveness of twin-pontoon floating structures, both free and anchored. They showed that wider spacing between pontoons reduced roll motion, though the heave response in free-floating systems behaved inversely. In addition, Chen et al. [12] revealed that a dual-pontoon floating breakwater is expected to be more appropriate for installation with a deeper draft. Moreover, Mohapatra et al., [13] considered a floating rectangular box-type structure and analyzed the responses of heave, sway, and roll motions. It was observed that the dimensions of the floating box hold considerable significance when evaluating wave forces, as the horizontal to vertical forces can vary markedly depending on the mode of oscillation, as well as the structural width and length. Further, Mohapatra and Soares [14] investigated a floating heaving box integrated with a vertical, flexible porous membrane positioned adjacent to the box. It was found that as the oblique angle increased, there was a corresponding decrease in vertical wave force damping and added mass coefficient. A recent review on motion responses, focusing on significant advancements and emerging techniques, was presented in [15].

The behavior of waves interacting with porous structures is another important research area, especially due to their role in shoreline protection, energy dissipation, and harbor safety. Early research highlighted the Tension Leg Platform (TLP) as a potential breakwater in [16], focusing on

the analysis of motion, especially surge response. Lee and Ker [17] conducted a motion analysis including a porous layer added to TLP to investigate the surge motion of the platform, considering the effects of porosity. Gayathri et al. [18] highlighted the importance of the structural thickness of porous barriers in enhancing wave energy dissipation. In a recent study, Sukcharoen et al. [19] proposed a pervious concrete to ecologically safeguard coastlines, highlighting the environmental benefits of its permeability.

Seabed topography also significantly influences wave dynamics and structural responses. Undulating seabeds can alter water flow patterns, affecting temperature, salinity, and hydrodynamic pressure distributions. Studies examining floating pontoons on undulating seabeds have notably shaped the six degrees of freedom of movements [20]. Trivedi and Koley [21] focused on evaluating the damping and added mass characteristics for a rectangular floating structure undergoing heave, pitch, and surge employing the Boundary Element Method (BEM). The study revealed that greater ripple amplitudes in the undulating seabed resulted in more pronounced oscillatory behavior in the radiation coefficients.

In the vicinity of employing floating structures, the integration of thread-like adhesives on top of intricate coastal structures brings in functional benefits. Their ability to stretch and adapt, along with their eco-friendly nature, gives fibrillar adhesives a distinct edge in coastal applications. Their adhesion relies on van der Waals forces, which become more effective when extensive contact areas are divided into smaller, flexible microstructures [22]. Geckos, known for their ability to adhere to surfaces of varying texture, inspired the development of fibrillar adhesives [23]. These adhesives outperform flat adhesives due to their capacity to conform to rough surfaces via independently deforming fibers [24]. Spolenak et al. [25] introduced "adhesion design maps" that support the development of optimized artificial adhesive systems, enhancing floating structure design. Li et al. [26] examined primary attributes of gecko adhesion, namely controllability, adaptability, and self-cleaning, for efficient fabrication and design of gecko-inspired dry adhesive surfaces. Recently, a few studies have delved into the intriguing world of bioinspired structures, focusing on innovative designs and mechanisms [27, 28]. Fibrillar adhesive breakwaters, designed for maximum energy dissipation, can be impacted by undulations in ways not accounted for in traditional models. The unique properties of fibrillar adhesives include their ability to absorb wave energy without permanent deformation, adhere to both smooth and rough surfaces, and exhibit significant elasticity. These characteristics have inspired their integration onto the surface of breakwaters. Ultimately, this may act as a multifunctional platform that can support structures such as floating bridges, airports, storage facilities, and recreational parks.

The present model distinguishes itself from existing floating breakwaters by incorporating bio-inspired fibrillar adhesive on the top of an intricate floating breakwater, a feature that has not been addressed in earlier studies. These fibrillar adhesives, which do not release chemical residues, are particularly relevant for environmental applications. Moreover, the essential physical characteristics of the fibrillar adhesive layer, such as surface roughness, flexibility, and material compliance, are pivotal elements of the breakwater's efficacy in hydrodynamic applications. The layer's flexibility affects its ability to conform to complex surfaces, absorb stresses, and maintain adhesion under dynamic wave loading. A lack of flexibility may cause the adhesive to become brittle, thereby reducing its ability to maintain a watertight seal to accommodate motion between the water and the structure. The roughness of a surface performs dual roles: it enhances the mechanical adhesion

between the fibrils and the substrate, while also influencing the local hydrodynamic drag. Kim et al. (2008) [29] examined the characteristics of hydrophilic and hydrophobic surfaces in relation to various contact angles. Their findings indicate that an increase in hydrophobicity corresponds with an enhancement in the adhesion force of fibrils, while hydrophilic surfaces provide significant improvements in adhesion. Further, material compliance, determined by the elastic modulus of the fibrillar structure, governs the processes of deformation and absorption of energy when subjected to different hydrodynamic pressures. Recently, Li et al. [30] examined a mushroom- like dry adhesive surface characterized by a diameter of 40 micrometer and a height of 80 micrometer, developed from polyvinyl siloxane. Utilizing 3D optical surface profiling, the average surface roughness of the mushroom-shaped cap was measured to be approximately 25 nanometer. This design creates a flexible peeling mechanism that induces concentrated stress for detachment. Thus, with these key properties, this bio-inspired approach offers enhanced grip, energy dissipation, and positional stability without substantially increasing system mass, marking an entirely novel paradigm in floating breakwater design.

This study focuses on the motion response analysis of a fibrillar adhesive floating breakwater located near a porous structure, situated at a finite distance from a Gaussian undulating seabed. The primary motivation is to explore how seabed undulations, frictional effects, and structural porosity influence the dynamic behavior of the breakwater. Particular attention is paid to added mass and radiation damping effects, which are critical for accurate modeling and performance prediction under wave-induced forces. The problem is addressed by employing multi-domain BEM as discussed in Section 3. Section 4 discusses the impact of critical governing factors (wave number, angle of the incoming wave, friction, porosity, number of seabed ripples, and ripple amplitude). The results, including motion responses and hydrodynamic coefficients, are discussed in detail. Major findings and conclusions are drawn in Section 5.

2. Mathematical formulation

This section presents the mathematical model and corresponding boundary conditions that govern the dynamic behavior of a fibrillar adhesive breakwater located near a porous structure, positioned away from the Gaussian oscillatory seabed. The layout of the physical model is schematically depicted in Figure 1. The problem is formulated using a Cartesian coordinate system, with the x-axis positioned horizontally at the free surface and the z-axis pointing upward in the vertical direction. Beyond the region of the undulating bed, the water depth is assumed to be uniform. The entire domain is partitioned into two separate regions: R_1, representing the fluid domain with the impermeable floating structure, and R_2, corresponding to the porous structure region. The Γ_{F_1} and Γ_{F_2} denotes the free surface boundaries, Γ_C and Γ_R represents the far-field boundaries, the fixed water depth seabed boundary is represented by Γ_B, the monotonically decreasing seabed boundary is represented by Γ_M, the porous structural boundaries is represented by Γ_{D_1}, and the boundary of fibrillar adhesive floating breakwater is represented by Γ_{D_2} as illustrated in Figure 1. The fluid is considered incompressible, inviscid, and irrotational. The flow is assumed to be time-harmonic, and hence a velocity potential exists and can be expressed as $\Psi_j(x, y, z, t) = Re[\psi_j(x, z)e^{-\mathrm{i}(k_y y-\omega t)}]$, where ω is the angular frequency, and k_y is the wave number in the y-direction. The dispersion relation with the progressive wave number k_0 is represented as $\omega^2 = gk_0 \tanh k_0 h$, where g is the acceleration due to

gravity, and h is the water depth. Since this study focuses on the radiation problem, the velocity potential $\psi_j(x, z)$ is subsequently decomposed as follows, (see [21]):

$$\psi_j = \sum_{q=1}^{3} \psi_j{}^q, \tag{2.1}$$

where $q = 1, 2$, and 3 represent the motions of surge, heave, and pitch, respectively. In addition, the velocity potential $\psi_j{}^q(x, z)$ of the radiated problem is represented as $\psi_j{}^q(x, z)$=$Re[-i\omega\phi_j{}^q(x, z)]$. The radiated velocity potential $\phi_j{}^q$ satisfies the Helmholtz equation in the fluid region,

$$(\nabla^2 - k_y{}^2)\phi_j{}^q(x, z) = 0. \tag{2.2}$$

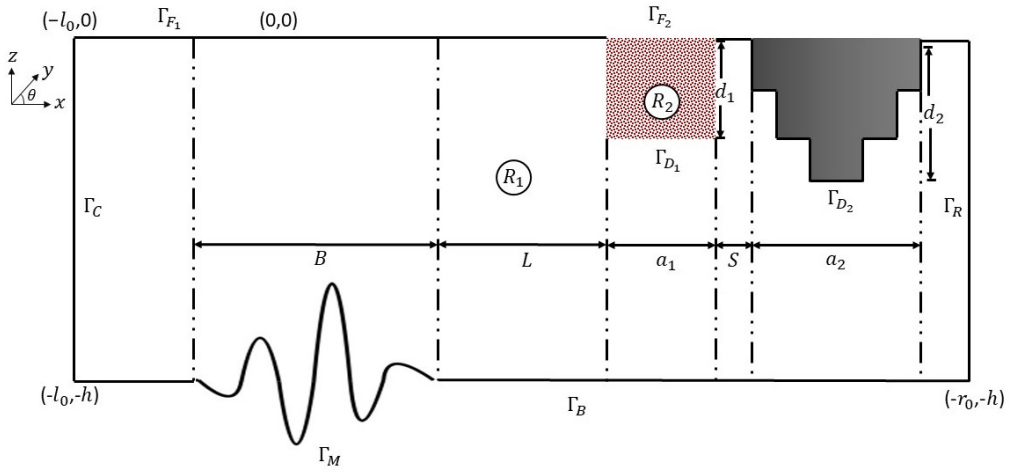

(a) Schematic diagram with the representation of boundaries.

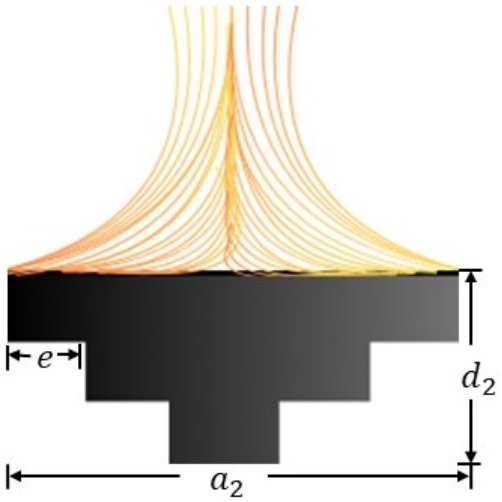

(b) Fibrillar Adhesive Floating Breakwater

Figure 1. Schematic representation of the present model.

The linearized boundary conditions of the free surface are given as in [31]:

$$\frac{\partial {\phi_1}^q}{\partial n} - K{\phi_1}^q = 0 \text{ on } \Gamma_{F_1}, \tag{2.3}$$

$$\frac{\partial {\phi_2}^q}{\partial n} - K(m - \mathrm{i}f){\phi_2}^q = 0 \text{ on } \Gamma_{F_2}, \tag{2.4}$$

where $K = \frac{\omega^2}{g}$, with g denoting a gravitational constant. Here, n is the outward-pointing normal, the inertial coefficient m is expressed as $m = 1 - \frac{1-\epsilon}{\epsilon}C$, where ϵ and C represent the porosity and added mass coefficient, and f is the friction coefficient as discussed in Chen et al. [32].

The added mass coefficient C is defined as in [33]:

$$C = \gamma_m \frac{1-\epsilon}{\epsilon}, \tag{2.5}$$

where $\gamma_m = 0.34$.

In the physical context, the added mass coefficient C denotes the ratio of the fluid's inertia, which must be accelerated alongside the structure, to the inertia of the displaced water. Moreover, waves interacting with porous media result in partial penetration of the incoming flow through the pores, leading to energy dissipation, viscous resistance, and a phase lag between the structural response and the hydrodynamic pressure field. This leads to a decrease in the effective added mass coefficient, as the body does not accelerate a continuous volume of fluid; rather, some fluid flows around the structure through the pores.

The boundary condition for the variable seabed elevation as in [34] is given by

$$\frac{\partial {\phi_1}^q}{\partial n} = 0 \text{ on } \Gamma_B,\ \Gamma_M. \tag{2.6}$$

The floating structure boundary representation as in [31] and [35], respectively, is expressed as

$$\frac{\partial \phi_1^q}{\partial n} = -\epsilon \frac{\partial \phi_2^q}{\partial n},\ \phi_1^q = (m - if)\phi_2^q \text{ on } \Gamma_{D_1}, \tag{2.7}$$

$$\frac{\partial \phi_1^q}{\partial n} = J_q \text{ on } \Gamma_{D_2} \text{ for } q = 1, 2, 3. \tag{2.8}$$

To determine the normal velocity J_q, it is assumed that the radiated potential ${\phi_j}^q$ describes the wave field resulting from oscillation in the qth mode, as presented in [35]

$$J_q = \begin{cases} n_x & \text{for } q = 1, \\ n_z & \text{for } q = 2, \\ r_z n_x - r_x n_z & \text{for } q = 3. \end{cases} \tag{2.9}$$

Finally, the far-field boundary in [21] is expressed as

$$\frac{\partial {\phi_1}^q}{\partial n} - ik_0 {\phi_1}^q = 0 \text{ on } \Gamma_C \text{ and } \Gamma_R, \tag{2.10}$$

3. Solution using multi-domain BEM

In this section, the formulated boundary value problem is analyzed using the multi-domain boundary element method. All boundary conditions are reformulated with respect to the outward normal vector along the boundaries. By applying Green's second identity to the velocity potential $\phi_j{}^q$ over the domain, with boundary Γ_j, and using the free space Green's function $G(x, z; x_0, z_0)$, we arrive at the following integral equation as in [36],

$$\frac{1}{2}\phi_j(x,z) = -\left(\int_\Gamma G\frac{\partial\phi_j}{\partial n} - \phi_j\frac{\partial G}{\partial n}\right) d\Gamma. \tag{3.1}$$

In this context, G represents the fundamental solution to the two-dimensional Helmholtz equation as defined in Eq 2.2. This Green's function $G(x, z, x_0, z_0)$ satisfies the following:

$$(\nabla^2 G - {k_y}^2 G)\phi_j(x,z) = \delta(x-x_0)\delta(z-z_0) = \delta(Q-Q_0), \tag{3.2}$$

where $Q(x, y)$,$Q_0(x_0, y_0) \in \Omega$ as discussed in [37] with

$$\delta(Q-Q_0)) = \begin{cases} 0, & Q \neq Q_0 \\ \infty, & Q = Q_0 \end{cases} \tag{3.3}$$

and

$$G(x,z;x_0,z_0) = -\frac{K_0(k_y r)}{2\pi}, \quad r = \sqrt{(x-x_0)^2 + (z-z_0)^2}, \tag{3.4}$$

where K_0 is the modified Bessel function of second-kind with zeroth-order. The Bessel function's recurrence formula as in [18] is defined as

$$\frac{\partial G}{\partial n} = \frac{k_y}{2\pi}K_1(k_y r)\frac{\partial r}{\partial n}, \tag{3.5}$$

where K_1 is the modified Bessel function of the second kind of first-order. Further, as $r \to 0$, we have the asymptotic equivalence [18],

$$K_0(k_y r) = -\gamma - \ln\frac{k_y r}{2}, \tag{3.6}$$

where $\gamma = 0.5772$ is Euler's constant. The aforementioned properties of the Green's function are discussed in [37]. Each boundary Γ_j is discretized into a finite segments, where both ϕ and its normal derivative ϕ_n are considered constant across each segment. Applying the boundary conditions from

Eqs (2.3)–(2.10) into Eq (3.1), we obtain the following system of integral equations as in [21],

$$\begin{aligned}
&\frac{1}{2}\phi_1^q + \int_{\Gamma_C}\left(\phi_1^q\frac{\partial G}{\partial n} - G\frac{\partial \phi_1^q}{\partial n}\right)d\Gamma + \int_{\Gamma_B}\frac{\partial G}{\partial n}\phi_1^q d\Gamma \\
&\quad + \int_{\Gamma_M}\frac{\partial G}{\partial n}\phi_1^q d\Gamma + \int_{\Gamma_R}\left(\phi_1^q\frac{\partial G}{\partial n} - G\frac{\partial \phi_1^q}{\partial n}\right)d\Gamma \\
&\quad + \int_{\Gamma_{D_1}}\left(\phi_1^q\frac{\partial G}{\partial n} - G\frac{\partial \phi_1^q}{\partial n}\right)d\Gamma + \int_{\Gamma_{D_2}}\frac{\partial G}{\partial n}\phi_1^q d\Gamma \\
&\quad + \int_{\Gamma_{F_1}}\left(\frac{\partial G}{\partial n} - KG\right)\phi_1^q d\Gamma = \int_{\Gamma_{D_2}} J_q G d\Gamma,
\end{aligned} \tag{3.7}$$

$$\begin{aligned}
&\frac{1}{2}\phi_2^q + \int_{\Gamma_{D_1}}\left(\frac{1}{m-\mathrm{i}f}\phi_1^q\frac{\partial G}{\partial n} - \frac{1}{\epsilon}G\frac{\partial \phi_1^q}{\partial n}\right)d\Gamma \\
&\quad + \int_{\Gamma_{F_2}}\left(\frac{\partial G}{\partial n} - K(m-\mathrm{i}f)G\right)\phi_2^q d\Gamma = 0 \text{ for } q = 1, 2, 3.
\end{aligned} \tag{3.8}$$

For computational purposes, the above integral equations are discretized into a matrix form as in [35],

$$\begin{aligned}
&\sum\left(H^{i,j} - ik_0 G^{i,j}\right)\phi_{1j}^q\Big|_{\Gamma_C} + \sum H^{i,j}\phi_{1j}^q\Big|_{\Gamma_B} + \sum H^{i,j}\phi_{1j}^q\Big|_{\Gamma_M} \\
&+ \sum\left(H^{i,j} - ik_0 G^{i,j}\right)\phi_{1j}^q\Big|_{\Gamma_R} \\
&+ \sum\left(H^{i,j}\phi_{1j}^q - \frac{\partial \phi_{1j}^q}{\partial n}G^{i,j}\right)\Bigg|_{\Gamma_{D_1}} + \sum H^{i,j}\phi_{1j}^q\Big|_{\Gamma_{D_2}} \\
&+ \sum\left(H^{i,j} - KG^{i,j}\right)\phi_{1j}^q\Big|_{\Gamma_{F_1}} = \sum G^{i,j}J_q\Big|_{\Gamma_{D_2}},
\end{aligned} \tag{3.9}$$

$$\begin{aligned}
&\sum\left(\frac{1}{m-\mathrm{i}f}H^{i,j}\phi_{1j}^q - \frac{1}{\epsilon}\frac{\partial \phi_{1j}^q}{\partial n}G^{i,j}\right)\Bigg|_{\Gamma_{D_1}} \\
&+ \sum\left(H^{i,j} - K(m-\mathrm{i}f)G^{i,j}\right)\phi_{2j}^q\Big|_{\Gamma_{F_2}} = 0 \text{ for } q = 1, 2, 3.
\end{aligned} \tag{3.10}$$

4. Results and discussion

This section focuses on the influence of an undulated seabed and a porous structure positioned near a fibrillar adhesive floating breakwater for different physical parameters. The discussion primarily addresses different radiation results as described in Section 2. In the context of the radiation problem, the added mass and damping components are key physical quantities, and their respective expressions

are given by

$$\tilde{A}_{q,k} = \rho \int_{\Gamma_{D_3}} Re[\phi^q] n_k d\Gamma \quad \text{for} \quad q = 1, 2, 3 \tag{4.1}$$

$$\tilde{N}_{q,k} = \rho\omega \int_{\Gamma_{D_3}} Im[\phi^q] n_k d\Gamma \quad \text{for} \quad q = 1, 2, 3, \tag{4.2}$$

where $n_1 = n_x$, $n_2 = n_z$, and $n_3 = r_z n_x - r_x n_z$. As presented in [21], the added mass and damping coefficients are non-dimensionalized as follows:

$$A_{1,1} = \tilde{A}_{1,1}/2\rho h^2, \; N_{1,1} = \tilde{N}_{1,1}/2\omega\rho h^2, \tag{4.3}$$

$$A_{2,2} = \tilde{A}_{2,2}/2\rho h^2, \; N_{2,2} = \tilde{N}_{2,2}/2\omega\rho h^2, \tag{4.4}$$

$$A_{3,3} = \tilde{A}_{3,3}/2\rho h^3, \; N_{3,3} = \tilde{N}_{3,3}/2\omega\rho h^3. \tag{4.5}$$

In the present study, the sea bed profile is provided as in [38]

$$\xi_b(x) = He^{\gamma x^2} \sin(k_b x), \; \frac{-M\pi}{k_b} \leq x \leq \frac{M\pi}{k_b}, \tag{4.6}$$

where γh^2 and $k_b h$ are the dimensionless amplitude decay factor and bottom wave number, respectively. The following parameters will remain unchanged throughout the investigation unless otherwise stated: water depth $h = 10$ meter, and oblique incident angle $\theta = 30°$. For Gaussian oscillatory sea bed, $\gamma h^2 = 0.05$, $k_b h = 2$, ripple amplitude $H/h = 0.16$, and number of ripples $M = 4$. For breakwaters, the heights are $d_1/h = 0.5$ and $d_2/h = 0.6$, the widths are $a_1/h = 0.5$ and $a_2/h = 1$, spacing between the porous structure and breakwater is $S/h = 0.5$, spacing between the undulated bed and porous structure is $L/h = 1$, the porosity is $\epsilon = 0.5$, inertial coefficient is $m = 1$, and friction of the porous structure is $f = 0.5$.

4.1. Convergence study

This subsection examines the convergence of solutions obtained through the multi-domain boundary element method for different values of porosity ϵ of the porous structure near the fibrillar adhesive floating breakwater. The selection of panel size for discrete elements is fundamental in determining the matrix dimensions. The adopted panel size P_s follows the formulation

$$P_s = \frac{h}{\kappa}, \tag{4.7}$$

while relating water depth h to the proportionality constant κ, as introduced by Zhao et al. [39]. This convergence study aims to reduce computational time while maintaining accuracy. Table 1 presents the computational results of added mass and damping coefficient of surge, heave, and pitch motions for porosity ϵ with varying κ. Further, $\kappa = 100$ is chosen for subsequent analysis, wherein the results converge with a precision of three decimal places.

Table 1. Convergence study of added mass and damping coefficients for fibrillar adhesive floating breakwater.

ϵ	κ	$A_{1,1}$	$N_{1,1}$	$A_{2,2}$	$N_{2,2}$	$A_{3,3}$	$N_{3,3}$
0.3	20	0.3482	0.2269	0.1862	0.3017	0.7573	0.3886
	40	0.3465	0.2233	0.1873	0.3035	0.7533	0.3847
	80	0.3458	0.2223	0.1884	0.3038	0.7521	0.3795
	100	0.3459	0.2225	0.1893	0.3039	0.7526	0.3784
0.5	20	0.2944	0.2172	0.1662	0.2574	0.6677	0.3731
	40	0.2934	0.2144	0.1674	0.2591	0.6643	0.3702
	80	0.2930	0.2136	0.1680	0.2591	0.6645	0.3660
	100	0.2929	0.2138	0.1687	0.2593	0.6646	0.3651
0.7	20	0.2640	0.2083	0.1576	0.2302	0.6168	0.3585
	40	0.2633	0.2058	0.1589	0.2317	0.6135	0.3560
	80	0.2629	0.2053	0.1591	0.2317	0.6131	0.3520
	100	0.2629	0.2051	0.1598	0.2315	0.6136	0.3512

4.2. Validation

Results for the added mass coefficient corresponding to surge and heave motions, obtained through the multi-domain BEM approach, are validated with established previous literature for a specific rectangular approximation from the fibrillar adhesive floating breakwater. This validation is achieved by minimizing the length $(a_2 - 3e)/h$ of the fibrillar adhesive floating breakwater, as shown in Figure 1(b) , to approximately zero, with the porous structure height set to $a_1/h = 0$ in the absence of an undulating seabed. Figure 2 shows the added mass associated with the surge and heave motion of the breakwater, plotted against the non-dimensional wave number k_0h. As observed, the lines indicate the current results obtained using the multi-domain BEM approach, and the symbols reflect the findings reported in [40]. The current results demonstrate good alignment with those found in the literature, thus validating the present approach.

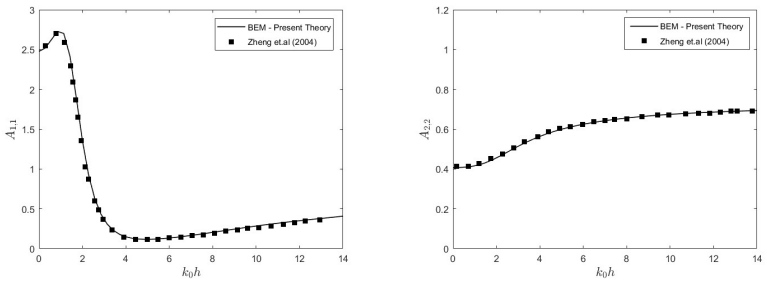

(a) (b)

Figure 2. Comparision of the present study with [40]; (a) surge added mass coefficient $A_{1,1}$ and (b) heave added mass coefficient $A_{2,2}$ versus wave number k_0h of a floating rectangular structure without undulated seabed fixed with $h/a_2 = 3$, $d_2/a_2 = 1$, and $\theta = 0°$.

4.3. *Effects of undulated seabed and porous parameters on added mass and damping coefficients*

Figure 3 demonstrates the variation of added mass and damping coefficient for motions of surge, heave, and pitch plotted as a function of wave number k_0h for different values of the friction coefficient f. In Figures 3(a), 3(b), and 3(c), the added mass corresponding to motions of surge $A_{1,1}$, heave $A_{2,2}$, and pitch $A_{3,3}$ increases as f decreases, particularly in intermediate wave conditions. This is because lower friction allows more energy to reach the breakwater, creating strong acceleration of water around the structure, leading to higher added mass. Further, Bragg resonance is observed near the primary Bragg value $k_0h \approx 1$. The oscillatory pattern, noticeable with Bragg resonance, is due to the presence of the Gaussian oscillatory seabed, where the standing waves are formed between the ripples of the undulating seabed. Resonance becomes more pronounced in the range $1.5 \leq k_0h \leq 2$, attributed to wave trapping between the porous structure and the fibrillar adhesive breakwater. In the confined zone, the cuts of the step-like fibrillar adhesive breakwater break the waves and reduce strong reflection. In the bandwidth of the Bragg resonance, all the damping coefficients associated with surge $N_{1,1}$, heave $N_{2,2}$, and pitch $N_{3,3}$ motions in Figure 3(d), 3(e), and 3(f), exhibit a trend opposite to that of added mass: as the friction coefficient f increases, the damping coefficients also increase. Consequently, the heave damping coefficient $N_{2,2}$ decreases rapidly as observed in [21]. Moreover, compared to surge motion, the pitch motion is highly damped.

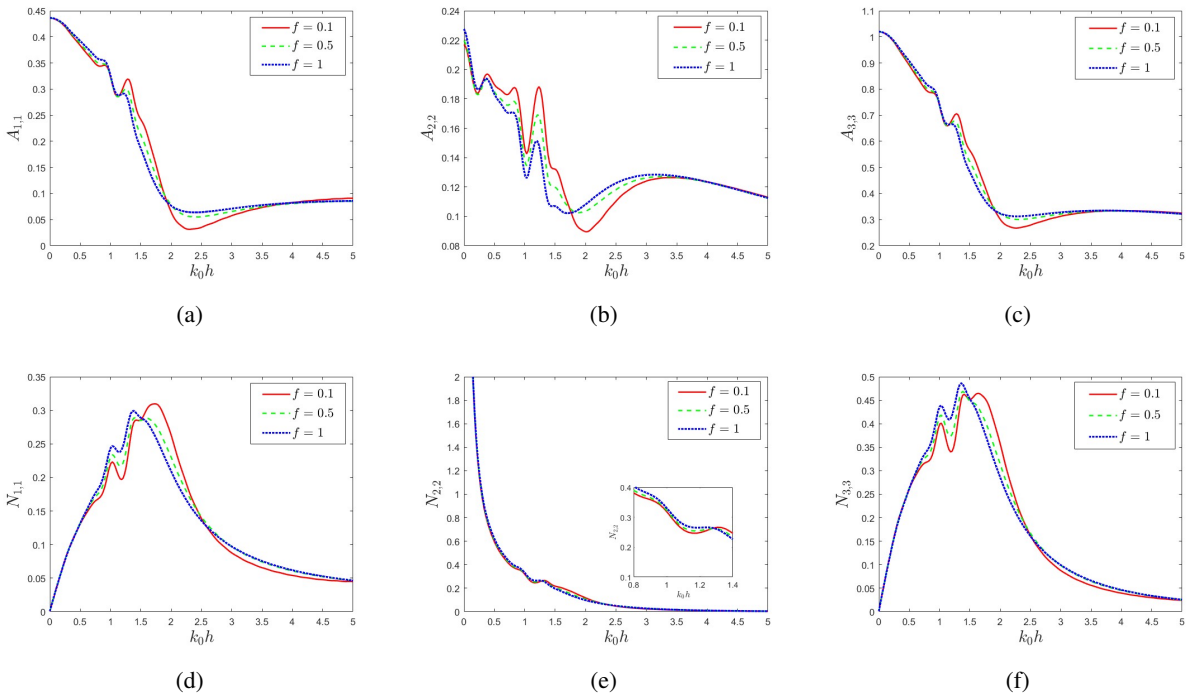

Figure 3. Variation in the (a) surge added mass $A_{1,1}$, (b) heave added mass $A_{2,2}$, (c) pitch added mass $A_{3,3}$, (d) surge damping $N_{1,1}$, (e) heave damping $N_{2,2}$, and (f) pitch damping $N_{3,3}$ coefficient versus wave number k_0h for various friction coefficients f of porous structure.

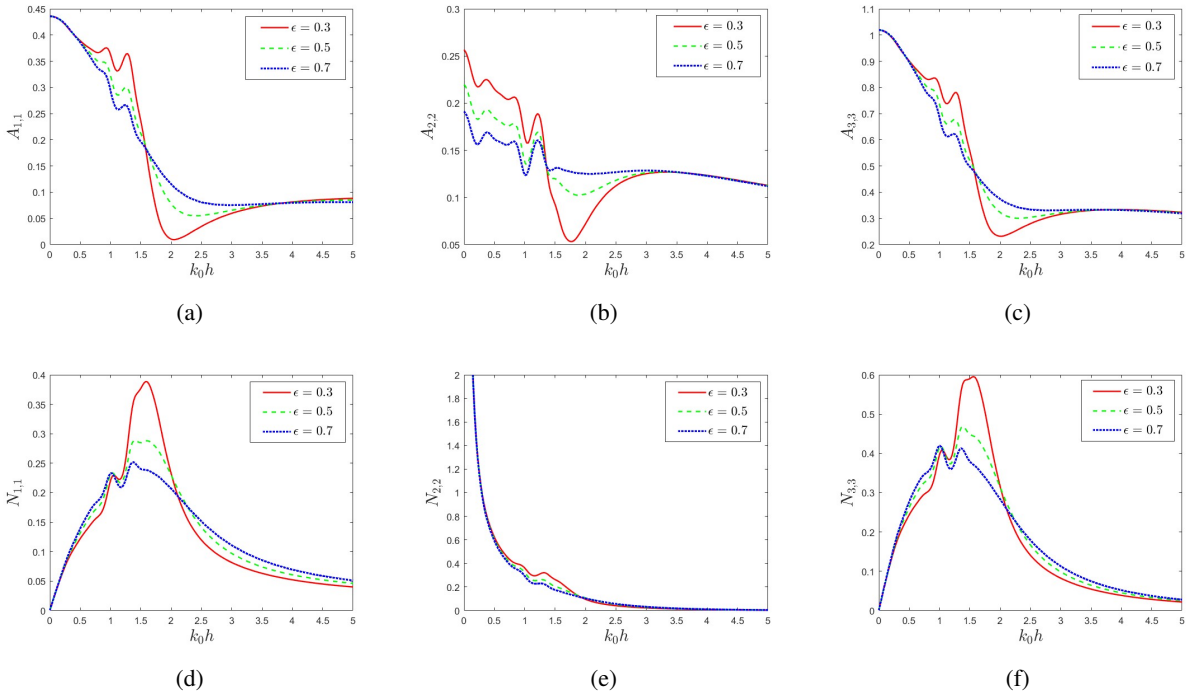

Figure 4. Variation in the (a) surge added mass $A_{1,1}$, (b) heave added mass $A_{2,2}$, (c) pitch added mass $A_{3,3}$, (d) surge damping $N_{1,1}$, (e) heave damping $N_{2,2}$, and (f) pitch damping $N_{3,3}$ coefficient versus wave number k_0h for various porosities ϵ.

Figure 4 illustrates the variation in added mass and damping for motions of surge, heave, and pitch plotted versus wave number k_0h for various porosity ϵ. As porosity ϵ decreases, the surge $A_{1,1}$, heave $A_{2,2}$, and pitch $A_{3,3}$ added mass increases in long and intermediate waves as in Figure 4(a), 4(b), and 4(c). This is because the porosity impact is minimal in the bandwidth of Bragg resonance as the Gaussian undulating bed is at a finite distance from the porous structure. However, the generation of standing waves between the porous layer and the fibrillar adhesive breakwater leads to resonance as observed in [35], which, in turn, causes the added mass for all motions to decrease as k_0h increases. For lower porosity ($\epsilon = 0.3$), the heave added mass $A_{2,2}$ attains a global dip in intermediate waves due to the pressure variation that occurs between the porous structure and fibrillar adhesive breakwater. In Figure 4(d) and 4(f), the surge $N_{1,1}$ and pitch $N_{3,3}$ damping increase with a decrease in porosity ϵ. At higher porosity ($\epsilon = 0.7$), the internal flow resistance of the porous medium decreases, leading to a reduction in energy dissipation via friction within the pores. As a result, the structure allows more wave energy to be transmitted rather than absorbed and dissipated. In Figure 4(e), the heave damping coefficient $N_{2,2}$ decreases rapidly in long waves. Furthermore, as porosity decreases, the heave damping coefficient $N_{2,2}$ increases in intermediate waves.

Figure 5 demonstrates the variation in added mass and the damping coefficient for motions of surge, heave, and pitch plotted versus wave number k_0h for various structural heights d_1/h of the porous structure. In Figure 5(a) and 5(c), surge $A_{1,1}$ and pitch $A_{3,3}$ added mass increase with an increase in structural height d_1/h in long waves. In Figure 5(b), the heave added mass $A_{2,2}$ attains a local dip near the primary Bragg value $k_0h \approx 1$ where no phase shift occurs as the structural height d_1/h varies. In Figure 5(d), the surge damping coefficient $N_{1,1}$ in intermediate waves increases as the height of porous

structure d_1/h increases. This is because the waves transmitted from the larger draft of the porous structure hit the step-like geometry, resulting in increased wave energy absorption and disrupting the flow, which leads to less sideward movement of the breakwater. As k_0h increases, the heave damping coefficient $N_{2,2}$ decreases rapidly, as can be seen in Figure 5(e). A decrease in the structural height of the porous structure d_1/h also leads to less damping of the heave motion in intermediate waves. Moreover, in Figure 5(f), pitch motion is damped more effectively as the porous structure gets deeper due to better disruption of wave-induced torque. Thus, proper positioning of a porous structure with optimal parameters could enhance the stability of the adjacent fibrillar adhesive breakwater.

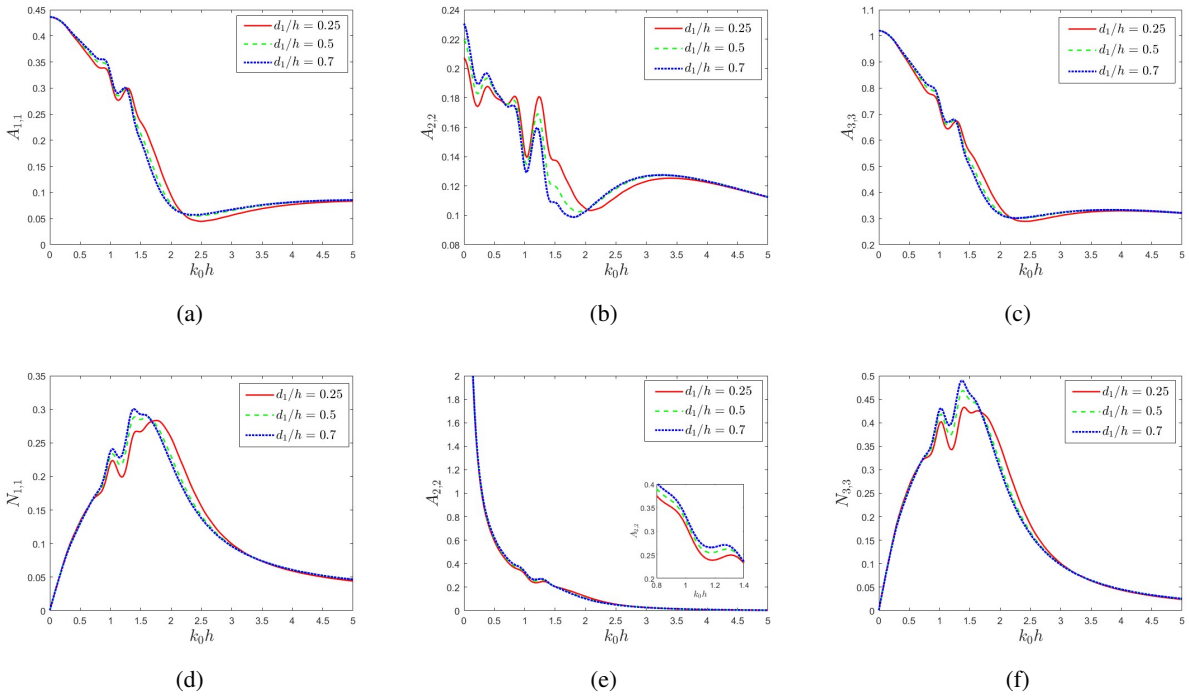

Figure 5. Variation in the (a) surge added mass $A_{1,1}$, (b) heave added mass $A_{2,2}$, (c) pitch added mass $A_{3,3}$, (d) surge damping $N_{1,1}$, (e) heave damping $N_{2,2}$, and (f) pitch damping $N_{3,3}$ coefficient versus wave number k_0h for various structural heights d_1/h of porous structure.

Figure 6 demonstrates the variation in added mass and damping coefficient for motions of surge, heave, and pitch plotted versus oblique angle θ for different numbers of ripples M. In Figure 6(a), 6(b), and 6(c), the added mass of surge $A_{1,1}$, heave $A_{2,2}$, and pitch $A_{3,3}$ motions increases in an oscillatory pattern for increasing oblique angle θ. In addition, as the number of ripples M increases, the phase shift becomes more evident. This is due to the back and forth movement of waves within the ripples of the non-uniform seabed [41]. Notably, in Figure 6(d), 6(e), and 6(f), the surge $N_{1,1}$, heave $N_{2,2}$, and pitch $N_{3,3}$ damping coefficient decreases in an oscillatory pattern for increasing oblique angle θ. Consequently, the oscillatory trend becomes more significant with an increase in ripple count M. This is because of the destructive or constructive interference within the crest of ripples. Further, for both added mass and damping coefficients for motions of surge, heave, and pitch, the oscillatory pattern is predominant for $\theta \leq 50^\circ$. This is due to the fact that the interaction of the incident wave with the non-uniform seabed modifies the phase velocity, producing oscillations at short angles θ.

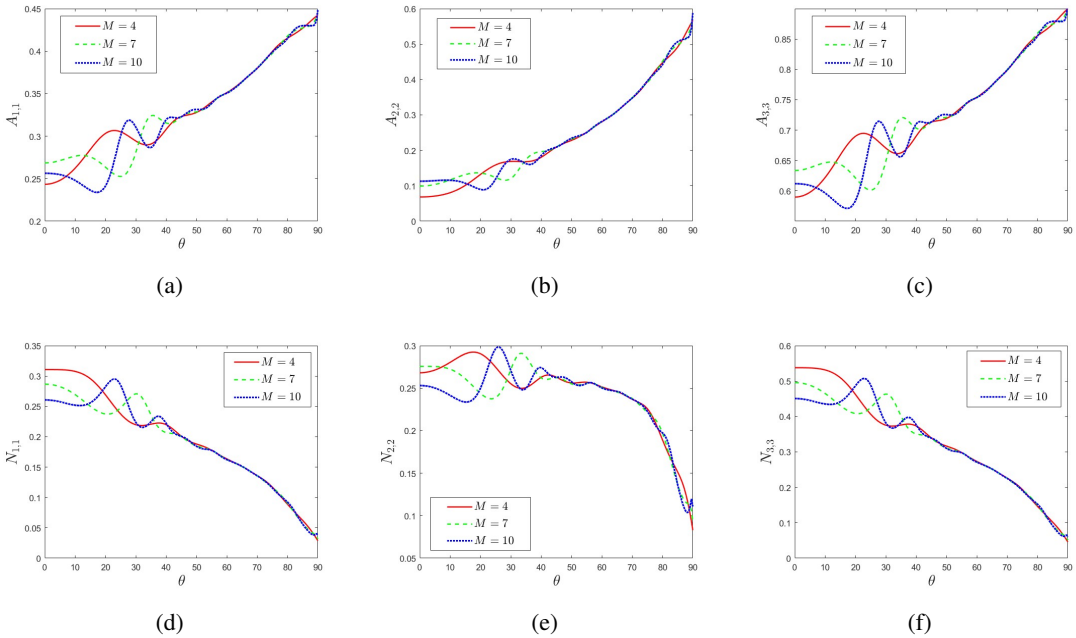

Figure 6. Variation in the (a) surge added mass $A_{1,1}$, (b) heave added mass $A_{2,2}$, (c) pitch added mass $A_{3,3}$, (d) surge damping $N_{1,1}$, (e) heave damping $N_{2,2}$, and (f) pitch damping $N_{3,3}$ coefficient versus oblique angle θ for various numbers of ripples M of undulated seabed.

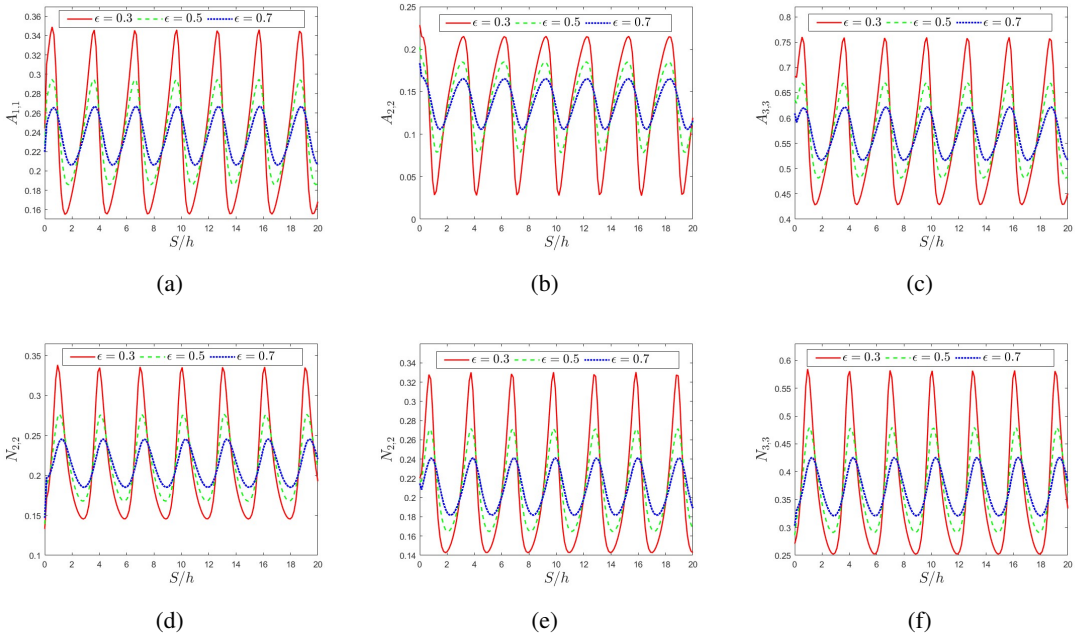

Figure 7. Variation in the (a) surge added mass $A_{1,1}$, (b) heave added mass $A_{2,2}$, (c) pitch added mass $A_{3,3}$, (d) surge damping $N_{1,1}$, (e) heave damping $N_{2,2}$, and (f) pitch damping $N_{3,3}$ coefficient versus gap distance between the porous structure and fibrillar adhesive breakwater S/h for various porosities ϵ.

Figure 7 depicts the variation in added mass and damping coefficient for motions of surge, heave, and pitch plotted versus S/h for different porosity values ϵ. The added mass and damping coefficient associated with surge, heave, and pitch motions increase as the porosity ϵ decreases. This is because the decrease in porosity confines the fluid motion, thus exhibiting a stronger inertia around the surrounding fluid between the porous structure and the fibrillar adhesive breakwater. In Figures 7(a), 7(c), and 7(e), the minima of surge added mass $A_{1,1}$, pitch added mass $A_{3,3}$, and heave damping $N_{2,2}$ shifts toward the right due to the inertial effect of porosity parameter ϵ. In Figure 7(b), the maxima of the heave added mass $A_{2,2}$ exhibits a leftward shift as a result of the constructive interference of the incoming wave. In Figures 7(d) and 7(f), minima of the surge $N_{1,1}$ and pitch $N_{3,3}$ damping is left shifting due to the fact that one portion of wave energy is dissipated by the porous structure while another portion is being trapped between the confined region of the porous structure and the fibrillar adhesive breakwater. The destructive and constructive interference of the interaction of waves between the porous structure and the fibrillar adhesive breakwater is the cause of the periodic oscillation in the added mass and damping coefficients.

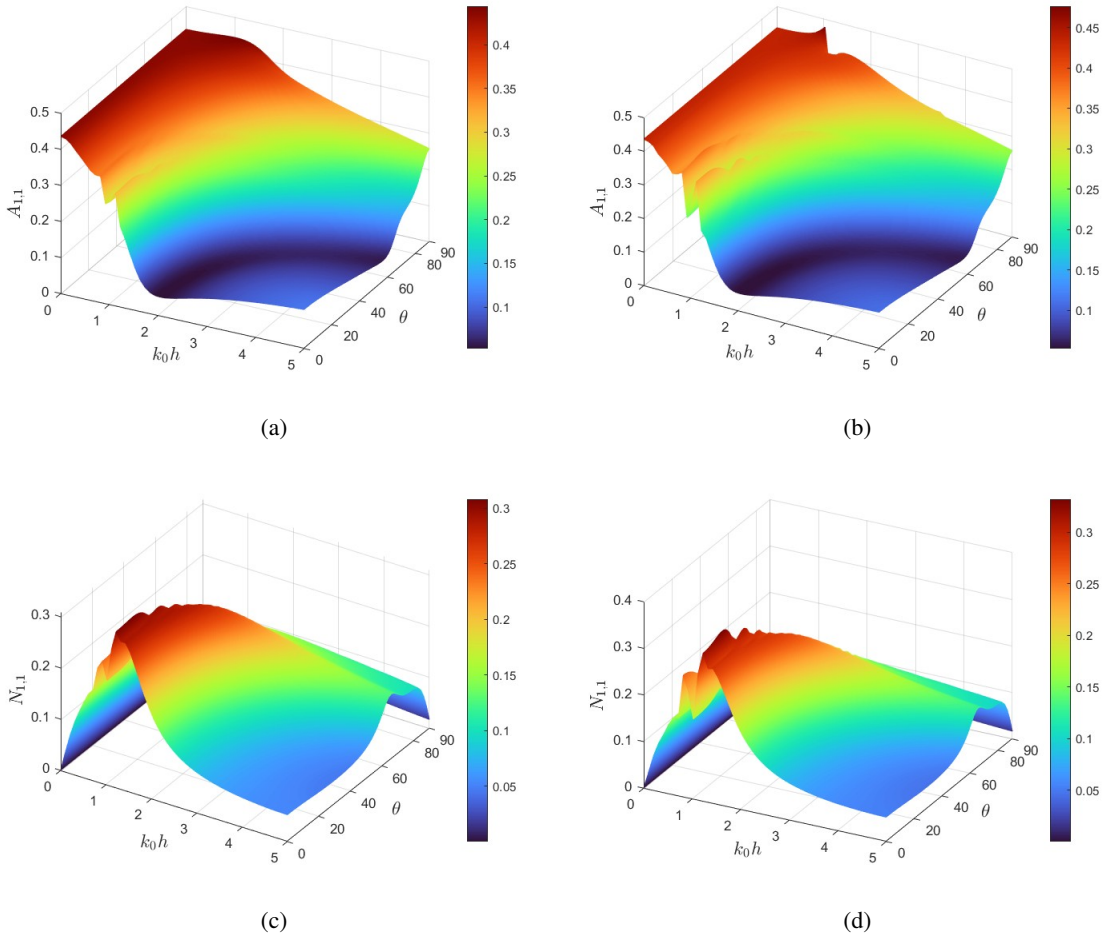

Figure 8. Surface plot of surge added mass $A_{1,1}$ for different ripple amplitude (a) $H/h = 0.16$ and (b) $H/h = 0.32$, and surge damping coefficient $N_{1,1}$ for (c) $H/h = 0.16$ and (d) $H/h = 0.32$ versus k_0h and θ.

In Figure 8, the surface plot depicting the surge radiation coefficients of the fibrillar adhesive floating breakwater for various values of (k_0h,θ) is examined for different ripple amplitudes H/h. As k_0h increases, the surge added mass $A_{1,1}$ decreases for both ripple amplitudes $H/h = 0.16$ and $H/h = 0.32$. However, the dip of the added mass curve near the primary Bragg value $k_0h \approx 1$ in the Bragg resonance bandwidth is more significant for ripple amplitude $H/h = 0.32$ as in Figure 8(b) compared to $H/h = 0.16$ in Figure 8(a). This is because, as the ripple amplitude H/h increases, the trapping of waves between the successive ripples of the Gaussian undulating seabed will be more predominant, resulting in intense oscillations. Further, as θ increases, the surge added mass $A_{1,1}$ increases. On the other hand, as k_0h increases, the surge damping coefficient $N_{1,1}$ grows in a bell-shaped oscillatory pattern. In addition, the primary Bragg peak $k_0h \approx 1$ in the surge damping curve $N_{1,1}$ is greater for $H/h = 0.32$ in Figure 8(d) than for $H/h = 0.16$ in Figure 8(c). This is because, as ripple amplitude increases, it modifies the drag force by generating flow circulation. As θ increases, the surge damping coefficient $N_{1,1}$ decreases.

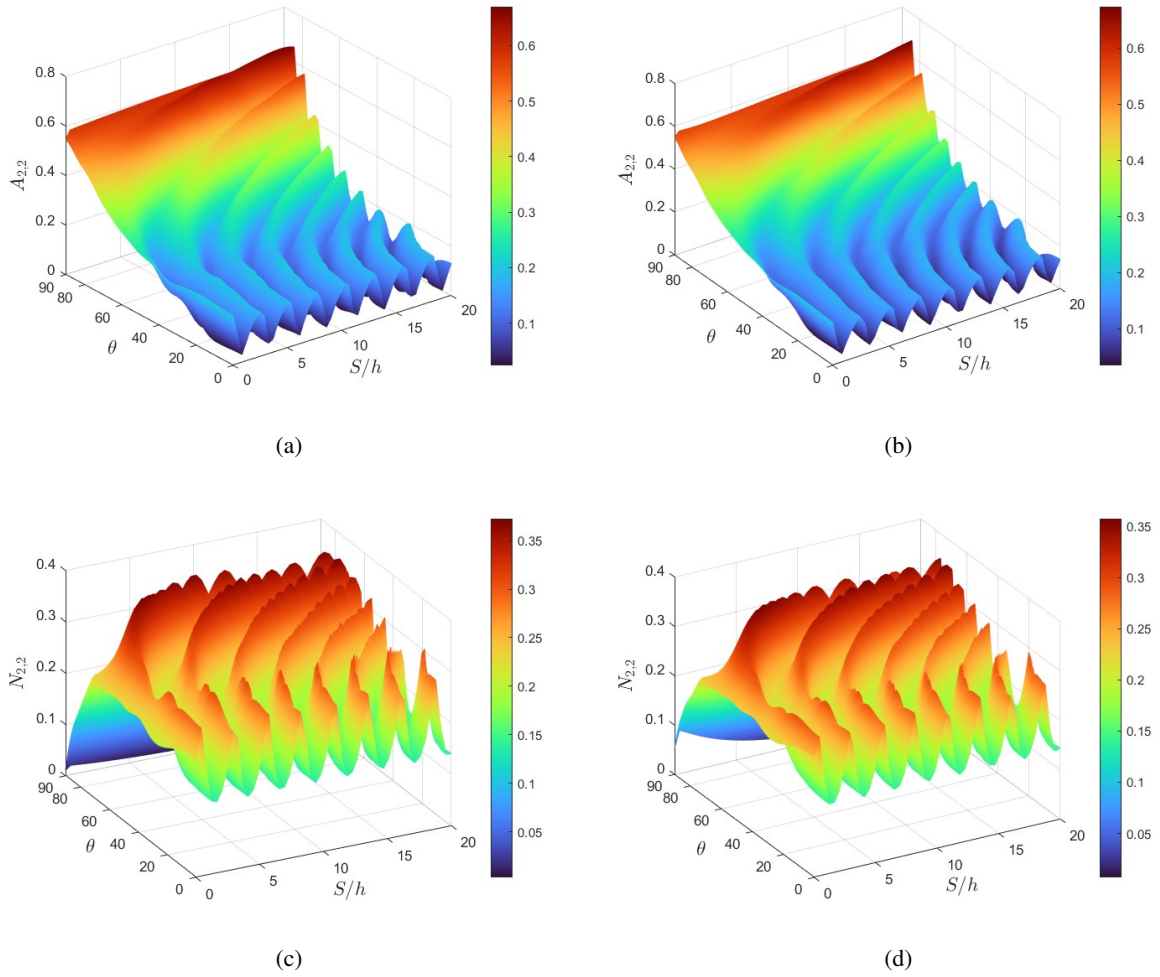

Figure 9. Surface plot of heave added mass $A_{1,1}$ for different friction coefficient (a) $f = 0.1$ and (b) $f = 0.5$, and heave damping coefficient $N_{1,1}$ for (c) $f = 0.1$ and (d) $f = 0.5$ versus S/h and θ.

In Figure 9, the surface plot depicting the heave radiation coefficients of the fibrillar adhesive floating breakwater for various values of (S/h,θ) is examined for different friction coefficients f. As S/h increases, the heave added mass $A_{2,2}$ exhibits a larger amplitude for a lower friction $f = 0.1$ in Figure 9(a) than for $f = 0.5$ in Figure 9(b). This is due to the impact of the lower friction of the porous structure on the step-like fibrillar adhesive breakwater, where the edges of the step-like geometry increase the additional mass of the surrounding fluid during up-down motion. The periodic oscillatory pattern increases as S/h increases. This is because waves are partially transmitted from the porous structure, along with the waves reflected from the fibrillar adhesive breakwater, resulting in a combined effect characterized by interference and phase shift. This oscillatory pattern is more prominent for a smaller oblique angle θ. Similar to heave added mass $A_{2,2}$, heave damping $N_{2,2}$ is higher for $f = 0.3$ in Figure 9(c) than for $f = 0.5$ in Figure 9(d). Higher heave damping is achieved for a larger oblique angle θ. In particular, the step-like edges of the fibrillar adhesive breakwater dissipate more energy when the waves interact, resulting in higher damping.

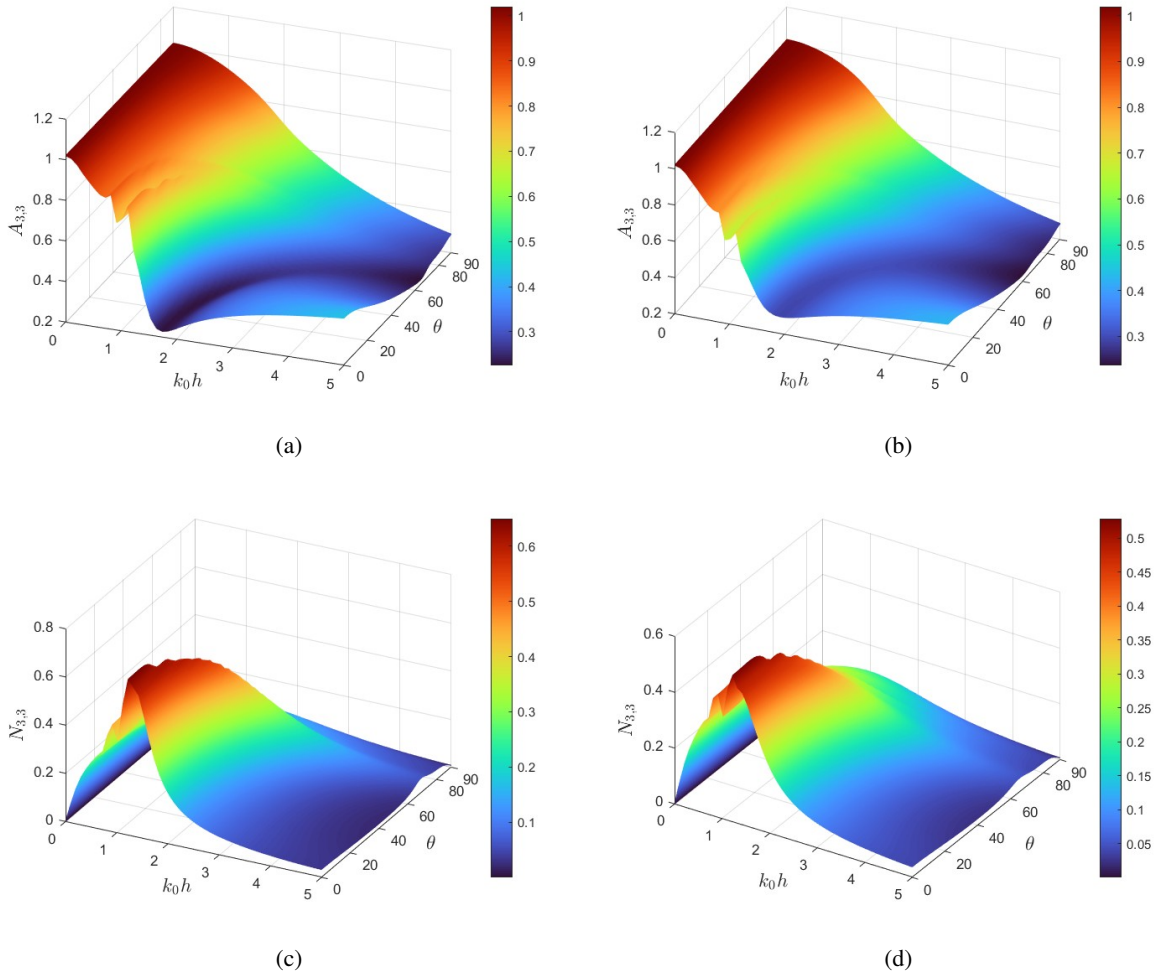

Figure 10. Surface plot of pitch added mass $A_{3,3}$ for different porosity (a) $\epsilon = 0.3$ and (b) $\epsilon = 0.5$, and pitch damping coefficient $N_{3,3}$ for (c) $\epsilon = 0.3$ and (d) $\epsilon = 0.5$ versus k_0h and θ.

In Figure 10, the surface plot depicting the pitch radiation coefficients of the fibrillar adhesive

floating breakwater for various values of (k_0h,θ) is investigated for different porosity ϵ. As k_0h increases, the pitch added mass $A_{3,3}$ decreases in intermediate waves exhibiting more significant resonance phenomenon for lower porosity $\epsilon = 0.3$ in Figure 10(a) than for $\epsilon = 0.5$ in Figure 10(b). This resonance occurs due to the entrapment of waves between the porous structure and the waves reflected from the cuts of the step-like face of the fibrillar adhesive breakwater. Pitch added mass $A_{3,3}$ decreases as θ increases. For lower porosity $\epsilon = 0.3$ in Figure 10(c), when the waves from the porous structures interact with the rotating breakwater, the complex pressure field that surrounds the breakwater reduces the oscillation with higher damping. This pitch damping curve narrows for increasing k_0h and exhibits greater damping compared to $\epsilon = 0.5$ in Figure 10(d). Further, as θ increases, the pitch damping coefficient $N_{3,3}$ increases.

5. Conclusions

In the present study, wave radiation from a fibrillar adhesive breakwater near a porous structure in the presence of the Gaussian oscillatory seabed is analyzed. To explore the physical problem, a multi-domain boundary element approach is employed. The added mass and radiation damping coefficients, the key hydrodynamic parameters in wave radiation, are studied for surge, heave, and pitch motions of the fibrillar adhesive floating breakwater. The key conclusions of the study are as follows:

- It is observed that as the non-dimensional wave number k_0h increases, the resonance peak of the added mass and damping coefficients for surge, heave, and pitch motions decrease with an increase in the friction coefficient f of the porous structure. This behavior is more pronounced at lower values of friction and porosity.
- The resonance phenomenon leads to a significant increase in the added mass at specific resonant frequencies, as the wave patterns induced by the seabed enhance wave trapping and energy accumulation.
- Consequently, the breakwater experiences high inertial forces attributed to the added mass, especially at resonant frequencies where the interaction between the seabed and waves is most significant. Furthermore, as porosity decreases, the surge and pitch motions are strongly damped in intermediate waves.
- For all three modes of motion (surge, heave, and pitch), the oscillatory patterns of added mass and damping coefficients are most pronounced for incident wave angles $\theta \leq 50^\circ$. As H/h increases, wave trapping between the successive ripples of the Gaussian undulating seabed causes an increase in the surge added mass and damping coefficient.
- Additionally, as the ripple count increases, the destructive or constructive interference within ripple crests induces a phase shift in the added mass and damping coefficients.
- It is also notable that the occurrence of the primary Bragg peak at $k_0h \approx 1$ is independent of variations in the friction coefficient, porosity, and structural height of the porous structure, and ripple amplitude and ripple count of the Gaussian oscillatory seabed.

In conclusion, the analysis shows that an optimal porous structure with parameters $d_1/h = 0.5$, $\epsilon = 0.5$, and $f = 0.5$ significantly enhances the added mass and damping coefficients of motion responses in the presence of an undulating seabed. Moreover, the intricate geometry of the fibrillar adhesive floating breakwater effectively scatters waves, thereby reducing nearshore wave energy. This reduction directly mitigates shoreline erosion and provides protection for coastal infrastructure. In

addition, the strong bio inspired adhesive interface improves structural integrity and stability while reducing relative motion and risk for detachment or breakage during extreme sea conditions. Further, the adhesive-based connection system is lightweight and enables the scaling or reconfiguration of breakwaters for diverse applications, such as marinas and aquaculture farms. However, this study does not attempt to physically validate the tangible features of the adhesive layer, because such investigations require an additional experimental framework and material assessment, which remain beyond the current scope. Nonetheless, this study constructs a thorough framework for understanding the wave attenuation effectiveness of the present model, particularly in relation to seabed topography and adjacent porous structures. Ultimately, this paper provides a robust groundwork for future explorations by highlighting wave-structure interaction and system-wide assessment of performance, paving the way for parametric studies and material optimization through experimental approach.

Appendix

A. Formulation of the Green's function for the modified Helmholtz equation

The Laplace equation can be expressed in cylindrical coordinates as

$$\nabla^2 = \frac{\partial^2}{\partial r^2} + \frac{1}{r}\frac{\partial}{\partial r}. \tag{A.1}$$

From Eq (3.2), the Helmholtz equation can be expressed as

$$\frac{\partial^2 G}{\partial r^2} + \frac{1}{r}\frac{\partial G}{\partial r} - k_y^2 G = \delta(r). \tag{A.2}$$

Multiplying both sides by r^2, we obtain

$$r^2\frac{\partial^2 G}{\partial r^2} + r\frac{\partial G}{\partial r} - r^2 k_y^2 G = r^2\delta(r). \tag{A.3}$$

Let us substitute $k_y r = x$, so that the above equation simplifies to the general form of the Bessel equation

$$\frac{x^2}{k_y^2}\frac{\partial^2 G}{\partial x^2}k_y^2 + \frac{x}{k_y}k_y\frac{\partial G}{\partial x} - \frac{x^2}{k_y^2}k_y^2 G = \frac{x^2}{k_y^2}\delta\left(\frac{x}{k_y}\right), \tag{A.4}$$

$$x^2\frac{\partial^2 G}{\partial x^2} + x\frac{\partial G}{\partial x} - x^2 G = 0. \tag{A.5}$$

Here, the right-hand side becomes zero because the Dirac delta function does not vanish only at $x = 0$.

Let $K_0(x)$ be the modified Bessel function of the second kind of zeroth order. This function is characterized by its singularity at the origin ($x = 0$) and its exponential decay for large values of x. It can be assumed that when $x \to \infty$, it is $K_0(x) = e^{-x}$, and when $x \to 0$, it is $K_0(x) = -\gamma - \ln(\frac{x}{2})$, where, $\gamma \approx 0.5772$ is the Euler's constant. Now, let $G = aK_0(k_y r)$. Integrating both sides of Eq (3.2), we obtain

$$\iint \nabla^2 G ds - \iint k_y^2 G ds = \iint \delta(r) ds = 1. \tag{A.6}$$

The second integral becomes zero when $x \neq 0$ (see [42]).

Now, transforming the first integral into a contour integral, we get

$$\begin{aligned}\iint \nabla^2 G ds &= \oint \nabla G.\hat{n} dL \\ &= \oint \frac{r}{\partial r}\left(-\gamma - ln\left(\frac{x}{2}\right)\right) a\hat{r} dL \\ &= \oint -\frac{1}{x}\frac{\partial x}{\partial r} a\hat{r} dL \\ &= \oint \frac{k_y}{k_y r} a\hat{r} dL \\ &= -\frac{a}{r}(2\pi r) \\ &= -2\pi a.\end{aligned}$$

From Eq A.6, we have,

$$\begin{aligned}-2\pi a &= 1, \\ (i.e.)a &= -\frac{1}{2\pi}.\end{aligned}$$

Hence,

$$G = -\frac{1}{2\pi} K_0(k_y r), \tag{A.7}$$

which is the Green's function for the zeroth order modified Helmholtz equation.

Author contributions

S. Sujana Praisilin: Writing – original draft, Software, Writing – review & editing; Chandru Muthusamy: Writing – original draft, Software, Writing – review & editing; Higinio Ramos: Writing – original draft, Software, Writing – review & editing. All authors contributed equally to the writing of this article. All authors have accepted responsibility for the entire manuscript content and approved its submission.

Use of AI tools declaration

The authors declare they have not used Artificial Intelligence (AI) tools in creating this article.

Funding information

Vellore Institute of Technology, Vellore, supported the work of MC under a SEED grant (Sanction Order No. SG20230081).

Acknowledgments

The authors gratefully acknowledge the valuable insights and stimulating discussions contributed by Dr. R. Gayathri of the Department of Mathematics, School of Advanced Sciences, Vellore Institute of Technology, Vellore, India, which have substantially enhanced the development of this work.

Conflict of interest

Professor Higinio Ramos is an editorial board member for AIMS Mathematics and was not involved in the editorial review or the decision to publish this article.

The authors declare that there is no conflict of interest regarding the publication of this manuscript.

References

1. R. W. Yeung, The transient heaving motion of floating eylinders, *J. Eng. Math.*, **16** (1982), 97–119. https://doi.org/10.1007/BF00042549
2. Y. He, B. Han, X. Han, H. Xie, Wave blocking performance of the symmetrical double-wing floating breakwater, *Ocean Eng.*, **303** (2024), 117852. https://doi.org/10.1016/j.oceaneng.2024.117852
3. S. Sujana Praisilin, R. Gayathri, M. Chandru, Effect of Trench Configuration on the Scattering and Radiation of Surface Gravity Waves by Different Floating Breakwaters, *Phys. Fluids*, **37** (2025), 087225. https://doi.org/10.1063/5.0278889
4. H. Y. Wang, Z. C. Sun, Experimental study on the influence of geometrical configuration of porous floating breakwater on performance, *J. Mar. Sci. Technol.*, **18** (2010), 13.
5. S. L. T. McGregor, Transdisciplinarity and biomimicry, *Transdisciplinary J. Eng. Sci.*, **4** (2013). https://doi.org/10.22545/2013/00042
6. P. Rakshit, S. Banerjea, Effect of bottom undulation on the waves generated due to rolling of a plate, *J. Mar. Sci. Appl.*, **10** (2011), 7–16. https://doi.org/10.1007/s11804-011-1035-8
7. C. C. Mei, J. L. Black, Scattering of surface waves by rectangular obstacles in waters of finite depth, *J. Fluid Mech.*, **38** (1969), 499–511. https://doi.org/10.1017/S0022112069000309
8. A. N. Williams, H. S. Lee, Z. Huang, Floating pontoon breakwaters, *Ocean Eng.*, **27** (2000), 221–240. https://doi.org/10.1016/S0029-8018(98)00056-0
9. S. Shafiuddin Amer, J. S. Mani, Performance of rigidly interconnected multiple floating pontoons, *J. Nav. Archit. Mar. Eng.*, **1** (2004), 1–15. https://doi.org/10.1061/40775(182)27
10. M. R. Gesraha, An eigenfunction expansion solution for extremely flexible floating pontoons in oblique waves, *App. Ocean Res.*, **26** (2004), 171–182. https://doi.org/10.1016/j.apor.2005.05.002
11. Diamantoulaki, Ioanna and Loukogeorgaki, Eva and Angelides, Demos C, 3D analysis of free and moored twin-pontoon floating breakwaters, *ISOPE Int. Ocean Polar Eng. Conf.*, (2007), ISOPE-I-07-395.
12. Y. Chen, Y. Liu, D. D. Meringolo, Comparison of hydrodynamic performances between single pontoon and double pontoon floating breakwaters through the SPH method, *China Ocean Engineering*, **36** (2022), 894–910. https://doi.org/10.1007/s13344-022-0078-8

13. S. C. Mohapatra, I. B. da Silva Bispo, Y. Guo, C. G. Soares, Analysis of wave-induced forces on a floating rectangular box with analytical and numerical approaches, *J. Mar. Sci. Appl.*, **23** (2024), 113–126. https://doi.org/10.1007/s11804-024-00385-7
14. S. C. Mohapatra, C. G. Soares, Wave energy system combined by a heaving box and a perforated flexible membrane wall, *J. Mar. Sci. Appl.*, (2025), 1–12. https://doi.org/10.1007/s11804-025-00696-3
15. S. P. Samuel, R. Gayathri, S. Koley, C. Muthusamy, Motion responses with hydrodynamic factors in designing a floating breakwater and wave energy converter: A review, *J. Ocean Eng. Mar. Energy*, **11** (2025), 233–263. https://doi.org/10.1007/s40722-024-00372-8
16. C. Lee, J. Lee, Wave-induced surge motion of a tension leg structure, *Ocean Eng.*, **20** (1993), 171–186. https://doi.org/10.1016/0029-8018(93)90033-E
17. C. Lee, W. Ker, Coupling of linear waves and a hybrid porous TLP, *Ocean Eng.*, **29** (2002), 1049–1066. https://doi.org/10.1016/S0029-8018(01)00065-8
18. R. Gayathri, M. B. M. Khan, H. Behera, Attenuation of wave force on a floating dock by multiple porous breakwaters, *Eng. Anal. Boundary Elem.*, **143** (2022), 170–189. https://doi.org/10.1016/j.enganabound.2022.06.002
19. T. Sukcharoen, D. Kositgittiwong, C. Ekkawatpanit, T. N. H. Tran, W.Tangchirapat, Assessment of the solitary wave attenuation through pervious concrete breakwater, *Constr. Build. Mater.*, **411** (2024), 134–457. https://doi.org/10.1016/j.conbuildmat.2023.134457
20. K.A. Belibassakis, A boundary element method for the hydrodynamic analysis of floating bodies in variable bathymetry regions, *Eng. Anal. Boundary Elem.*, **32** (2008), 796–810. https://doi.org/10.1016/j.enganabound.2008.02.003
21. K. Trivedi, S. Koley Effect of varying bottom topography on the radiation of water waves by a floating rectangular buoy, *Fluids*, **6** (2021), 59. https://doi.org/10.3390/fluids6020059
22. E. Arzt, S. Gorb, R. Spolenak, From micro to nano contacts in biological attachment devices, *Proc. Natl. Acad. Sci.*, **100** (2003), 10603–10606. https://doi.org/10.1073/pnas.1534701100
23. K. Autumn, Y. A. Liang, S. T. Hsieh, W. Zesch, W. P. Chan, T. W. Kenny, et al., Adhesive force of a single gecko foot-hair, *Nature*, **405** (2000), 681–685. https://doi.org/10.1038/35015073
24. M. P. Murphy, S. Kim, M. Sitti, Enhanced adhesion by gecko-inspired hierarchical fibrillar adhesives, *ACS Appl. Mater. Interfaces*, **1** (2009), 849–855. https://doi.org/10.1021/am8002439
25. R. Spolenak, S. Gorb, E. Arzt, Adhesion design maps for bio-inspired attachment systems, *Acta biomater.*, **1** (2005), 5–13. https://doi.org/10.1016/j.actbio.2004.08.004
26. X. Li, D. Tao, H. Lu, P. Bai, Z. Liu, L. Ma, et al., Recent developments in gecko-inspired dry adhesive surfaces from fabrication to application, *Surf. Topogr.: Metrol. Prop.*, **7** (2019), 023001. https://doi.org/10.1088/2051-672X/ab1447
27. J. Zhao, N. Xia, L. Zhang, A review of bioinspired dry adhesives: From achieving strong adhesion to realizing switchable adhesion, *Bioinspir. Biomim.*, **19** (2024), 051003. https://doi.org/10.1088/1748-3190/ad62cf
28. M. Li, Y. Sun, B. Bi, T. Wang, L. Shi, X. Wang, Bio-and bioinspired textures for enhancing friction forces, *Surf. Topogr.: Metrol. Prop.*, **13** (2025), 013003. https://doi.org/10.1088/2051-672X/adad8b
29. T. W. Kim, B. Bhushan, The adhesion model considering capillarity for gecko attachment system, *J. R. Soc. Interface*, **5** (2008), 319–327. https://doi.org/10.1098/rsif.2007.1078

30. X. Li, P. Bai, X. Li, L. Li, Y. Li, H. Lu, et al., Robust scalable reversible strong adhesion by gecko-inspired composite design, *Friction*, **10** (2022), 1192–1207. https://doi.org/10.1007/s40544-021-0522-4
31. S. Koley, H. Behera, T. Sahoo, Oblique wave trapping by porous structures near a wall, *J. Eng. Mech.*, **141** (2015), 04014122. https://doi.org/10.1061/(ASCE)EM.1943-7889.0000843
32. H. Chen, C. Tsai, J. Chiu, Wave reflection from vertical breakwater with porous structure, *Ocean Eng.*, **33** (2006), 1705–1717. https://doi.org/10.1016/j.oceaneng.2005.10.014
33. M. R. A. V. Gent, *Wave interaction with permeable coastal structures*, PhD Thesis, Delft University of Technology, 1995.
34. K. Panduranga, S. Koley, Water waves scattering by cylindrical dual porous floating breakwaters connected with a rectangular porous box and floating over an undulated seabed, *Meccanica*, **56** (2021), 3001–3024. https://doi.org/10.1007/s11012-021-01442-z
35. K. G. Vijay, S. Koley, K. Trivedi, C. S. Nishad, Hydrodynamic coefficients of a floater near a partially reflecting seawall in the presence of an array of caisson blocks, *J. Offshore Mech. Arct. Eng.*, **144** (2022), 021906. https://doi.org/10.1115/1.4052635
36. S. Koley, K. Panduranga, N. Almashan, S. Neelamani, A. Al-Ragum, Numerical and experimental modeling of water wave interaction with rubble mound offshore porous breakwaters, *Ocean Eng.*, **218** (2020), 108218. https://doi.org/10.1016/j.oceaneng.2020.108218
37. Katsikadelis, John T, *The boundary element method for engineers and scientists: Theory and applications*, Academic Press, 2016.
38. D. Goyal, T. K. Hota, S. C. Martha, Propagation of nonlinear surface waves over non-periodic oscillatory bottom profiles, *Eur. J. Mech.-B/Fluids*, **104** (2024), 194–214. https://doi.org/10.1016/j.euromechflu.2023.12.003
39. Y. Zhao, Y. Liu, H. Li, A. Chang, Iterative dual BEM solution for water wave scattering by breakwaters having perforated thin plates, *Eng. Anal. Boundary Elem.*, **120** (2020), 95–106. https://doi.org/10.1016/j.enganabound.2020.08.008
40. Y. H. Zheng, Y. G. You, Y. M. Shen, On the radiation and diffraction of water waves by a rectangular buoy, *Ocean Eng.*, **31** (2004), 1063–1082. https://doi.org/10.1016/j.oceaneng.2003.10.012
41. A. K. Mohapatra, K. G. Vijay, T. Sahoo, Bragg scattering of surface gravity waves by a submerged wavy porous plate, *Ocean Eng.*, **219** (2021), 108273. https://doi.org/10.1016/j.oceaneng.2020.108273
42. M. M. Jins, K. G. Vijay, V. Venkateswarlu, H. Behera, Oblique wave interaction with a floating dock in the presence of inverted trapezoidal pile-rock breakwaters, *Eng. Anal. Boundary Elem.*, **172** (2025), 106111. https://doi.org/10.1016/j.enganabound.2024.106111

AIMS Press